JGR Atmospheres

Key Points:

- Continuous ground surface temperature data for China were estimated by filling the gaps arising from the inconsistent measurement systems
- The overall mean annual ground surface temperature increased by $0.20 \pm 0.02°C$ dec^{-1} across China during 1956–2022
- Ground surface temperature warming was amplified by about 0.24°C dec^{-1} (or 70.6%) in winter since 1970 due to increased snow depth

Consistent Ground Surface Temperature Climatology Over China: 1956–2022

Shengdi Wang[1,2] , **Bin Cao[1]** , **Jiansheng Hao[3], Wen Sun[1], and Kun Zhang[4]**

[1]Key Laboratory of Tibetan Plateau Earth System Science, Environment and Resources (TPESER), National Tibetan Plateau Data Center, Institute of Tibetan Plateau Research, Chinese Academy of Sciences, Beijing, China, [2]Key Laboratory of Western China's Environmental Systems (Ministry of Education), College of Earth and Environmental Sciences, Lanzhou University, Lanzhou, China, [3]Key Laboratory of Land Surface Pattern and Simulation, Institute of Geographic Sciences and Natural Resources Research, Chinese Academy of Sciences, Beijing, China, [4]School of Geospatial Engineering and Science, Sun Yat-sen University, Zhuhai, China

Abstract The ground surface represents the land-atmosphere interface and plays a crucial role in exchanging energy, matter, and biochemical fluxes. The ground surface temperature (T_s) is hence widely investigated as an indicator to understand the thermal state of soil in a warming world. However, regular and continuous T_s measurements are rare worldwide, and the early T_s records were derived from snow surface measurements and are not comparable with the measurements of modern automatic systems. In this study, we reconstruct the T_s records of the China Meteorological Administration (CMA) for 1956–2022 by numerical simulation. The results show that the mean annual ground surface temperature (MAGST) during 1981–2010 ranged from 0.4 to 30.8°C at 632 stations. The MAGST was mainly controlled by air temperature and refined by snow depth. The overall MAGST increased by $0.20 \pm 0.02°C$ dec^{-1} across China during 1956–2022 and showed pronounced interdecadal variability corresponding to the surface air temperature ($0.23 \pm 0.03°C$ dec^{-1}). At the snow-covered sites, the T_s warming was amplified by increased snow depth, leading to about 0.24°C dec^{-1} (or 70.6%) faster warming for T_s in winter compared to that of surface air temperature. Many of the early reported ground surface temperature studies based on CMA measurements did not consider the measurement inconsistency and likely overestimated the warming trend of ground surface temperature over China.

Plain Language Summary Ground surface temperature (T_s) affects a variety of temperature-related phenomena on the Earth's surface and is hence widely investigated as an indicator to understand the interaction of land-atmosphere in a warming climate. However, continuous T_s measurements are rare worldwide. Restricted by the early measurement conditions, the early T_s records were recorded manually from the snow surface, and are not comparable with the measurements of the modern automatic systems. Therefore, we reconstructed a T_s time series for the China Meteorological Administration (CMA) data for 1956–2022 by numerical simulation. Our results show that the mean annual ground surface temperature (MAGST) increased by 0.20°C dec^{-1} across China during 1956–2022. The MAGST was mainly controlled by air temperature and refined by snow depth. T_s warming was amplified by about 0.24°C dec^{-1} (or 70.6%) in winter by increased snow depth since 1970, compared to the surface air temperature. Many of the early reported T_s studies based on CMA measurements did not consider the measurement inconsistency and likely overestimated the warming trend of T_s over China.

1. Introduction

The thermal state of soil varies in response to many climatic and topographic factors, including near-surface air temperature (Cao et al., 2018), vegetation cover (Cermak et al., 2017), precipitation (Magnússon et al., 2022), soil moisture (Zwieback et al., 2019), and snow cover (Cao et al., 2020; Zhang, 2005). Various processes, such as hydrological processes (Jin et al., 2009), vegetation growth (Kumar & Shekhar, 2015), infrastructure construction (Hjort et al., 2018), and landscape features (Streletskiy et al., 2017), are strongly dependent on the nature and temperature of the soil.

The ground surface represents the land-atmosphere interface and plays a crucial role in the exchange of energy, matter, and biochemical fluxes. The ground surface temperature (T_s) fluctuates in response to high-frequency variations in large-scale atmospheric circulation and fine-scale surface conditions. It is hence widely investigated as an indicator to understand the thermal state of soil under a warming world (Burke et al., 2020; Smith et al., 2022; Zhang et al., 2018). In addition, T_s measurements are commonly used to calibrate models' surface

energy balance components or as an upper boundary for soil hydrothermal process simulation (Gisnås et al., 2014; Sun et al., 2022). Despite the importance, regular T_s measurements, especially long-term time-series measurements, are relatively rare and often unavailable in most regions.

Since the 1950s, routine T_s measurement has been conducted by the China Meteorological Administration (CMA) (Wang et al., 2015). T_s was manually obtained from the bare ground (i.e., at a depth of 0.03 m) or the snow surface, if seasonal snow was present, and mercury thermometers were typically used (CMA, 2013; Gilichinsky et al., 1998). The temperature recorded in this way represents the land surface temperature (LST, e.g., snow surface during snow-covered periods) rather than T_s, although the variable name was assigned as T_s in the CMA records. Since 2000, the manual observation system of the CMA has gradually advanced to an automatic one (Cui et al., 2020). These systems differ in their T_s measurement when the ground is covered by snow, T_s is taken from the surface of the ground beneath the snow in the automatic system using a platinum resistance sensor. The CMA data sets do not include any correction to account for the change in measurement methodology, leading to the T_s records of the CMA being inconsistent (Cao et al., 2023; Liao et al., 2019; Wang et al., 2017).

A few studies have reported that, at the stations with snow cover, the automatically measured daily T_s can be up to about 15°C warmer than the manual measurements, which can be attributed to the snow insulation effects (Cui et al., 2020; Du et al., 2020; Zhang, 2005). However, this issue has either been ignored or inaccurately interpolated as being consistent across T_s measurements, and soil climate warming since 2000 has been overestimated over China (Cao et al., 2023; Wang et al., 2018; Zhang et al., 2016). Only very limited studies considered the inconsistency. For example, Du et al. (2020) and Xu et al. (2019) developed a semi-physical statistical model to derive homogenized T_s records. However, these algorithms lack an explicit expression of the influences of snow cover on soil thermal state and cannot be applied in T_s restruction at a high-temporal resolution. To understand the T_s climatology over China, long-term consistent ground surface records that fill the measurement gaps are required.

In this study, we aimed to: (a) produce consistent T_s records for the CMA stations over China for 1956–2022 via numerical simulation; and (b) investigate the soil climatology and the controlling factors based on the corrected records. The outputs of this study will provide a unique opportunity to analyze the thermal state of soil change and its response to climate change over China and could be extended to wider regions using a similar T_s measurement algorithm.
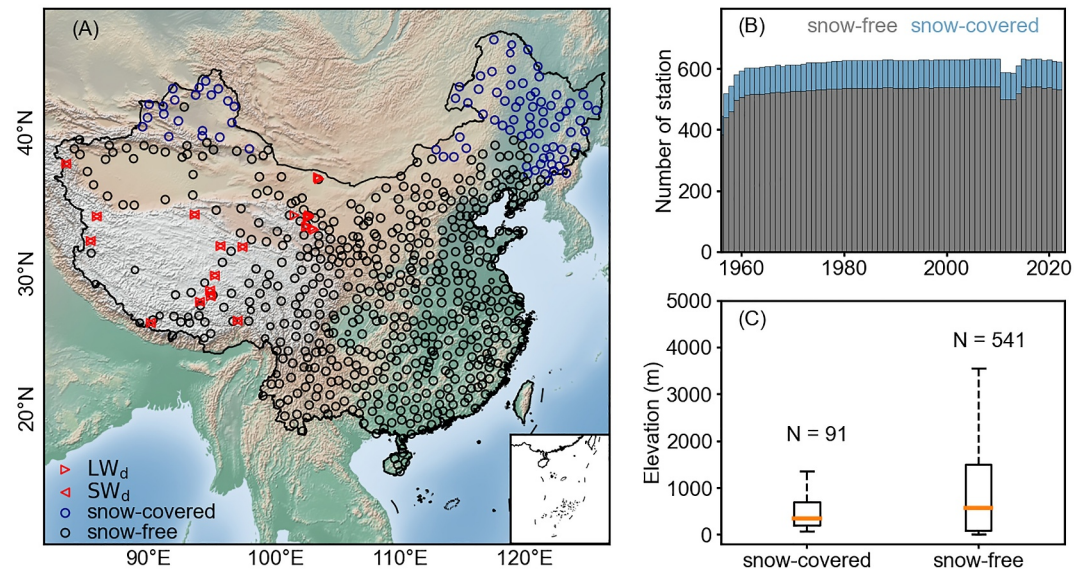
2. Observations

2.1. CMA Observations

The daily T_s records from 632 CMA stations were used in this study for model evaluation (Figure 1a; Table 1). Since the T_s observations before 2007 were derived from snow surface measurements (Figure 2, Cui et al., 2020), only the measurements after that were used to evaluate the simulated ground surface temperature (T_s^{mod}). To investigate the T_s changes and to force the process-based model, daily observations of near-surface air temperature (T_a), air pressure (airP), and snow depth (HS) were also used in this study (Table 1). The data cover the period from 1956 to 2022, but not all the data are available in a single year (Figure 1b). Note that the earlier period was not involved here as the CMA station was relatively limited at low altitudes (Peng et al., 2017). The CMA stations cover a wide elevation range of about 0–4900 m, and a variety of terrain (Figures 1a and 1c). The strong influence of seasonal snow on the thermal state of soil has been extensively investigated (Zhang, 2005). The CMA observations were hence divided into snow-covered and snow-free sites, to distinguish the controlling factors of T_s changes. In this study, a site with a stable snow-covered period, that is, the mean consecutive snow-covered day was ≥30 days during the measured period, was classified as a snow-covered station following Zhang and Zhong (2014).

2.2. Radiation Observations

Surface downwelling longwave (LW_d) and shortwave radiation (SW_d) data were required for the model forcing, but these observations were not available in the CMA network. They were hence derived from the ERA5 reanalysis, and the downscaled LW_d and SW_d (see Section 3.1) were evaluated at 24 and 12 additional stand-alone sites, respectively (Figure 1a; Table 1). The stand-alone observations of LW_d were from Ma et al. (2020); Zhu et al. (2021); Zhao, Zou, et al. (2021), while the SW_d was from Ma et al. (2020); Zhao, Zou, et al. (2021). The

Figure 1. (a) The distribution of the China Meteorological Administration (CMA) stations across China. (b) The number of stations with observations of both the air temperature and snow depth observations. (c) The elevation distribution of stations grouped by snow-covered conditions. The size of the symbols in (a) represents the year of the measurements, with a maximum of 67 years and a minimum of 18 years.

radiation observations covered the period of 2004–2018. The outliers of the observation time series were removed by visual checking.

3. Methods

3.1. Process-Based Model

A process-based model considering the surface energy balance and heat transfer was used to derive consistent T_s (Figure 2). The process of the surface energy balance is composed of solar radiation (downwelling), longwave radiation (downwelling and upwelling), latent heat, sensible heat, and conduction heat flux through the snow cover and ground surface:

$$(1 - \alpha)SW_d + LW_d + LW_u + Q_h + Q_e + Q_c = 0 \tag{1}$$

where α is the land surface albedo, LW_u is the emitted longwave radiation (W m^{-2}), Q_h is the sensible heat (W m^{-2}), Q_e is the latent heat (W m^{-2}), Q_c is the conduction heat flux through the snow cover and ground surface (W m^{-2}).

Table 1
List of Used Observations, Including Near-Surface Air Temperature (T_a), Air Pressure (airP), Snow Depth (HS), Ground Surface Temperature (T_s), Downwelling Longwave Radiation (LW_d), and Downwelling Shortwave Radiation (SW_d)

Measurements	Coverage	N	Purpose	Source
T_a	1956–2022	632	Forcing and downscaling evaluation	China Meteorological Administration
airP	1956–2022	632	Forcing	China Meteorological Administration
HS	1956–2022	632	Model input	China Meteorological Administration
T_s	2007–2022	632	Model evaluation	China Meteorological Administration
LW_d	2004–2018	24	Downscaling evaluation	Ma et al. (2020); Zhao, Zou, et al. (2021); Zhu et al. (2021)
SW_d	2004–2018	12	Downscaling evaluation	Ma et al. (2020); Zhao, Zou, et al. (2021)

Note. N means the station number.
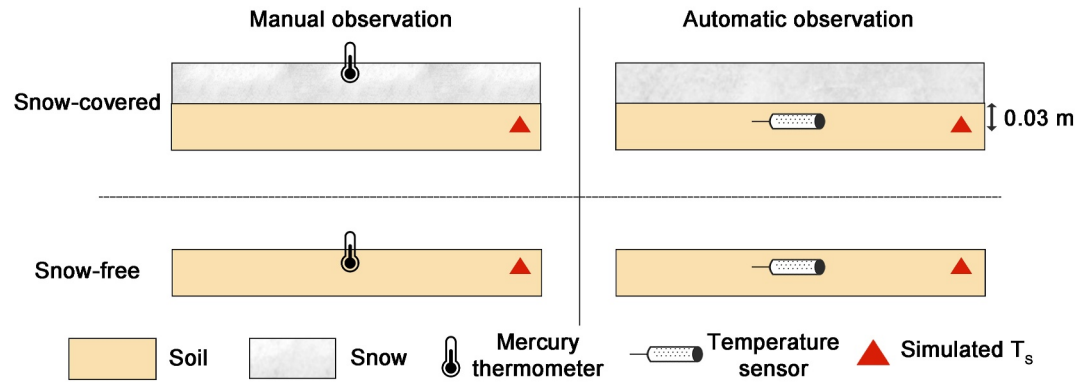
Figure 2. Observation instruments and methods for ground surface temperature (T_s) measurement. This figure is revised from Cui et al. (2020). The 0.03 m means the simulated soil temperature depth, corresponding to the manually measured depth.

The influence of snow cover on the soil thermal regime was considered by incorporating the heat transfer equation to calculate the surface heat balance. The heat transfer process is as follows:

$$C\frac{\partial T}{\partial t} = \frac{\partial}{\partial x}\left(\lambda_s \frac{\partial T}{\partial x}\right) \tag{2}$$

where T is the soil temperature (K), C is the apparent soil volumetric heat capacity (J m^{-3} K^{-1}), λ_s is the soil thermal conductivity (W m^{-1} K^{-1}), x is the depth (m) from the ground surface downward, and t is the timestep in day.

3.2. Model Parameterization and Setting Up

The land surface albedo (α) was set as either bare ground albedo ($\alpha_b = 0.2$, Ling & Zhang, 2004) or snow surface albedo (α_{sn}), depending on the snow cover condition. The α_{sn} was calculated as a function of the difference between the timestep since the last significant snowfall occurred (more than 1.0 cm) following Dee et al. (2011); Westermann et al. (2016). For non-melting conditions, α_{sn} decreases linearly with timestep, while an exponential decrease is assumed for melting conditions:

$$\alpha_{\mathrm{sn},t} = \begin{cases} \alpha_{\mathrm{sn},t-1} - 0.008 \cdot t, \; non-melting \\ \alpha_{\min} + \exp(-0.24 \cdot t)(\alpha_{\mathrm{sn},t-1} - \alpha_{\min}), \; melting \end{cases} \tag{3}$$

where $\alpha_{\max} = 0.85$ is the fresh snow albedo, $\alpha_{\min} = 0.50$ is the old snow albedo (Dee et al., 2011; Westermann et al., 2016).

LW_u was given from Stefan-Boltzmann law as:

$$LW_u = -\epsilon \sigma T_{s0}^4 \tag{4}$$

where ϵ is the ground surface emissivity, σ is the Stefan-Boltzmann constant (W m^{-1} K^{-4}), and T_{s0} (K) is the soil temperature of the first layer of discretized soil profiles, that is, at the soil depth of 0.03 m (Figure 2). The ground surface emissivity was set to 0.98 for the snow-covered period and 0.92 otherwise (Ling & Zhang, 2004).

The sensible heat flux was given from a common parameterization scheme (Walter et al., 2005):

$$Q_h = \rho_a C_p D_h (T_a - T_{s0}) \tag{5}$$

where ρ_a is the density of the air (kg m^{-3}), C_p is the specific heat of air, assumed to be 1003.5 J K^{-1} kg^{-1}, D_h is the exchange coefficient for sensible heat following Ling and Zhang (2004).

The latent heat flux was calculated using the model developed by Priestley and Taylor (1972) and Boike et al. (2008):

$$Q_e = \frac{\alpha_{pt}\Delta(Q_n - Q_c)}{\Delta + \gamma} \tag{6}$$

where Q_n is net radiation near the surface, α_{pt} is the Priestley–Taylor coefficient, Δ is the slope of the saturation vapor pressure-temperature curve (kPa K^{-1}) following Dingman (2015), γ is psychrometric constant (kPa K^{-1}) following Brunt (2011). Regarding α_{pt}, Priestley and Taylor (1972) reported 1.26 is reasonable for water and open grassland surfaces, and it has been used in numerous studies for a variety of ecosystems. However, α_{pt} was found to be site-specific and significantly controlled by near-surface soil moisture as well as vegetation conditions (Barton, 1979; Fisher et al., 2005; Martens et al., 2017; Miralles et al., 2011). For the bare ground of the CMA station, the algorithm from GLEAM was introduced here (Martens et al., 2017) and the maximum α_{pt} for is assumed to be 1.04 following Barton (1979); Fisher et al. (2005).

$$\alpha_{pt} = \min\left[1.26 \cdot \left(1 - \frac{\theta_c - \theta_w}{\theta_c - \theta_p}\right), 1.04\right] \tag{7}$$

where θ_w (%) is soil moisture, $\theta_c = 30\%$ is critical soil moisture, and $\theta_p = 5\%$ is soil moisture of wilting point following Miralles et al. (2011); Martens et al. (2017); Purdy et al. (2018). To reduce the possible uncertainty, soil moisture was derived as an ensemble mean of; six soil moisture products (ASCAT, AMSR2-JAXA, SMOS-BEC, SMOS-IC, SMAP-L3, CCI SM) (Zhang et al., 2022). The model assumed a constant soil water content as the mean from May to September during 2010–2018.

Q_c was given as:

$$Q_c = -(T_{s0} - T_s)\left(\frac{HS}{\lambda_{sn}} + \frac{z_0}{\lambda_s}\right)^{-1} \tag{8}$$

where T_s is the ground surface temperature (K), and z_0 was set to 0.03 m corresponding to the diameter of a mercury ball thermometer (Figure 2). λ_{sn} and λ_s are the snow and soil thermal conductivity (W m^{-1} K^{-1}).

The λ_{sn} was considered to be solely dependent on snow density (ρ_{sn}, kg m^{-3}) following Douville et al. (1995):

$$\lambda_{sn} = \lambda_i\left(\frac{\rho_{sn}}{\rho_i}\right)^{1.88} \tag{9}$$

where λ_i is the ice thermal conductivity of 2.2 W m^{-1} K^{-1}, ρ_i is the ice density of 920 kg m^{-3}. Static snow density is assumed here and was set to 200 kg m^{-3} based on the stand-alone in situ measurements (Cao et al., 2023; Zhong, Zhang, Su, et al., 2021).

The soil thermal conductivity was treated as a mixture of the volumetric fractions (θ) of soil minerals (m), water (w), ice (i), and air (a) following Cosenza et al. (2003):

$$\lambda_s = \left[\theta_m\sqrt{\lambda_m} + \theta_w\sqrt{\lambda_w} + \theta_i\sqrt{\lambda_i} + \theta_a\sqrt{\lambda_a}\right]^2 \tag{10}$$

where soil air content (θ_a) is set as 5%. During the soil freezing period, soil ice content (θ_i) is set as the soil water content minus the unfrozen water content (Equation 13). Soil mineral thermal conductivity (λ_m) was set to 2.92 W m^{-1} K^{-1} for the bare ground (Cao, et al., 2019, 2023; Ling & Zhang, 2004). While λ_m is variable, our sensitivity experiments indicated that λ_m has a minimal influence on the simulated T_s at the shallow depth of 0.03 m (not shown). The water and air thermal conductivity (λ_w and λ_a) were set to 0.56 W m^{-1} K^{-1} and 0.025 W m^{-1} K^{-1}, respectively.

The soil heat capacity for the soil process that accounts for the latent heat of freezing and melting of water/ice was given as:

$$C = C_s + L\frac{\partial \theta_w}{\partial T} \tag{11}$$

$$C_s = C_m\theta_m + C_w\theta_w + C_i\theta_i + C_a\theta_a \tag{12}$$

where C_s is soil volumetric heat capacity (J m^{-3} K^{-1}), and L is the volumetric latent heat of melting for ice (J m^{-3}). Similar to the soil thermal conductivity, the volumetric heat capacity of the soil was obtained by considering the mixture of minerals, water, ice, and air.

When the soil was frozen, the unfrozen water or super-cooled water was parameterized following Niu and Yang (2006):

$$\theta_w = \theta_{sat}\left\{\frac{10^3 L(T - T_{frz})}{gT\psi_{sat}}\right\}^{-\frac{1}{b}} \tag{13}$$

where θ_{sat} is the saturated soil moisture (%), g is the acceleration due to gravity of 9.8 m s^{-2}, T_{frz} is the freezing point temperature (273.15 K), ψ_{sat} is the saturated soil matric potential depending on the soil material properties, and b is the Clapp–Hornberger parameter. The soil material property information from Shangguan et al. (2013) was used in this study.

For the profile of the model, we used 5-layer snow, 16-layer soil at 0–1 m, and 90-layer soil at 1–10 m. A lower boundary condition of zero heat flux was used for the simulation. The first 5 years of the model forcing were used to spin up the model by running it 20 times (100 years) before the simulation.

3.3. Model Forcing and Downscaling

The model forcing includes T_a, LW_d, SW_d, wind speed, and airP. While T_a and airP are from the CMA network, the other atmospheric forcing, including: LW_d, SW_d, and wind speed are from ERA5 as they are not available in the CMA network. Note that data gaps were found for CMA observations, and ERA5 was used to fill the gap. Despite the inherent uncertainties, ERA5 was found to improve significantly compared to its predecessor, that is, ERA-Interim (He et al., 2021), and was demonstrated to be suitable for process-based simulations (i.e., Graham et al., 2019; Tarek et al., 2020). The original ERA5 data are subject to a coarse spatial resolution (0.25° or 31 km, Hersbach et al., 2020), and hence cannot capture the strong spatial variability arising from complex terrain (Figures 1a and 1c). For this reason, the ERA5 was downscaled by adopting the method of Fiddes and Gruber (2014), Cao et al. (2017), Cao, Zhang, et al. (2019). This method conducts elevation and topography correction (slope, aspect, and sky viewer factor) for SW_d and additionally considers the vertical variation of the cloud composition of the all-sky radiance for LW_d. A 3-D statistical downscaling method was used to produce T_a and airP via solving the lapse rate based on the pressure-level data sets. The downscaling scheme has been successfully applied in the complex terrain, that is, the Alps (Fiddes et al., 2015; Fiddes & Gruber, 2014) and the Tibetan Plateau (Cao et al., 2017; Martin et al., 2023).

3.4. Snow Depth Correction

The measured HS at the CMA stations was used as the model input, and the missing daily data were filled using the calibrated HS from ERA5. This is because the original ERA5 snow depth was reported to be biased due to the unsuitability of snow densification (Cao et al., 2020). The ERA5 HS was calibrated using the observations at each station. This was achieved by conducting a linear fitting between the observed HS and that from ERA5. Note that if the calibrated HS is smaller than 1 cm, it is set as 0 cm.

3.5. Model Evaluation

The downscaled T_a and the calibrated HS from ERA5 were evaluated against the CMA stations. The downscaled LW_d and SW_d from ERA5 were evaluated against the stand-alone sites (see Sec.2.2), respectively. The mean bias (BIAS) and root-mean-square error (RMSE) are introduced here as evaluation metrics:
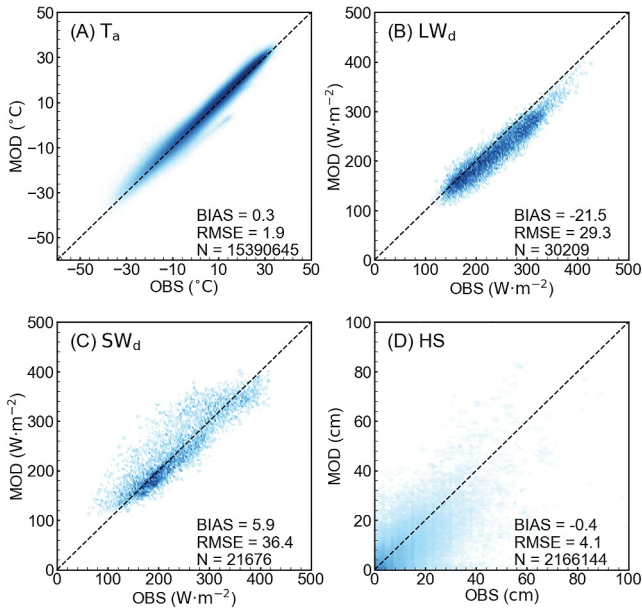
Figure 3. Evaluation of the downscaled daily (a) air temperature (T_a), (b) downwelling longwave radiation (LW_d), (c) downwelling shortwave radiation (SW_d) from ERA5, and (d) calibrated daily snow depth (HS) from ERA5. N is the number of measurements used for the evaluation.

$$BIAS = \frac{1}{N}\sum_{i=1}^{N}(mod - obs) \quad (14)$$

$$RMSE = \sqrt{\frac{\sum_{i=1}^{N}(mod - obs)^2}{N}} \quad (15)$$

where N is the total number of measurements, and mod and obs are modeled and observed variables, respectively.

4. Results

4.1. Evaluation

4.1.1. Downscaled Model Forcing

Benefiting from the well-resolved lapse rate, the downscaled T_a shows a good agreement with the observations at the 632 CMA stations, with the bias and RMSE being 0.3°C and 1.9°C, respectively (Figure 3a). In other words, the RMSE of downscaled T_a was reduced by 1.0°C compared to the original ERA5. The ERA5 radiation products also guarantee the accuracy of the radiation forcing. The bias of the downscaled daily LW_d is −21.5 W m^{-2} and the RMSE is 29.3 W m^{-2} (Figure 3b). The bias of the downscaled daily SW_d is 5.9 W m^{-2} and the RMSE is 36.4 W m^{-2} (Figure 3c). The downscaled radiation is found to significantly reduce the ERA5 uncertainty and be comparable to the satellite-based estimates/retrieval (e.g., Jiang et al., 2020; Tang et al., 2023).

The results demonstrate that there is generally a good agreement between the calibrated ERA5 HS and the observations, with the bias being about −0.4 cm and an RMSE of 4.1 cm (Figure 3d). The calibrated HS from ERA5 is also consistent with the observations (not shown). Overall, the evaluation results indicate that the downscaled meteorological variables and calibrated HS are generally consistent with the observations and can be used as suitable forcing/inputs for the numerical simulation.

4.1.2. Simulated Ground Surface Temperature

The results indicate that T_s^{mod} agrees with the observed ground surface temperature (T_s^{obs}) well, with the bias about 0.8°C and the RMSE ranging from 2.8 to 1.5°C at different temporal scales from daily to annually (Figures 4a and 4b). The simulated mean annual ground surface temperature (MAGST) is generally close in both the snow-free and snow-covered sites (Figure 5, RMSE = 1.6°C *vs.* 1.4°C). The surface offset (SO, as $T_s - T_a$) in winter, which describes the influences of the snow layer on the soil thermal regime, shows a slight bias of 0.1°C and an RMSE of 2.4°C. They both indicated the suitability of the model for capturing snow insulation effects (Figure 4c). Among
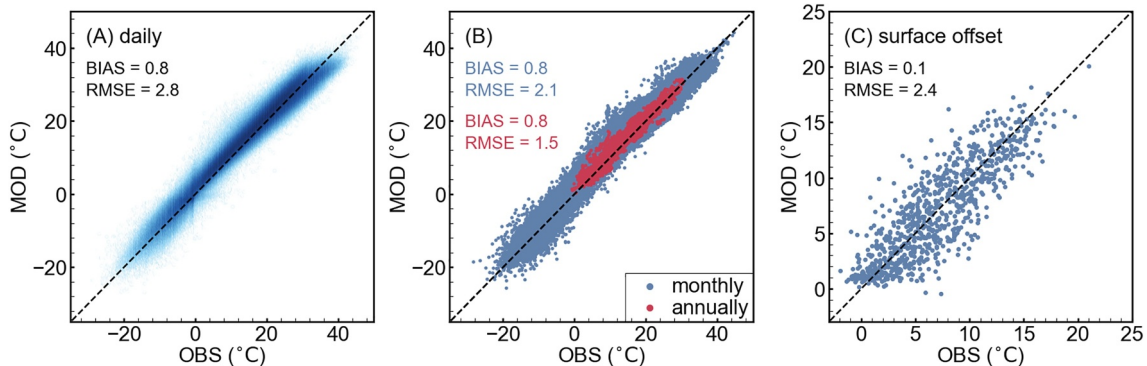
Figure 4. Evaluation of the simulated ground surface temperature (T_s^{mod}) with the observations (T_s^{obs}) at daily, monthly, and annual scales (a and b), and the simulated surface offset (SO) at the snow-covered sites (c). The evaluations were conducted using observations from the automatic system for 2007–2022.
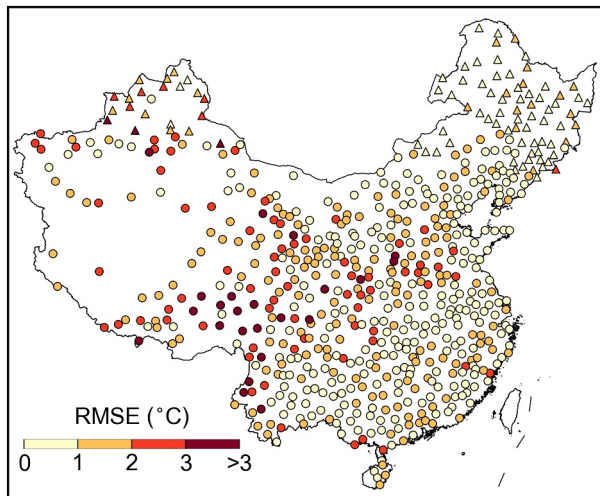
Figure 5. The RMSE of the simulated mean annual ground surface temperature (MAGST). The evaluation was conducted using the ground surface temperature from the automatic measurement system for 2007–2022. The triangle and circle symbol represent the snow-covered and snow-free station, respectively.

the 632 CMA stations, 83.5% have an RMSE of less than 2°C for MAGST; 66.8% of the stations have an RMSE of less than 2°C at a monthly scale; and 76.3% of the stations have an RMSE of less than 3°C at a daily scale (Figure 5). The evaluation results indicate the suitability of the process-based model to produce consistent T_s.
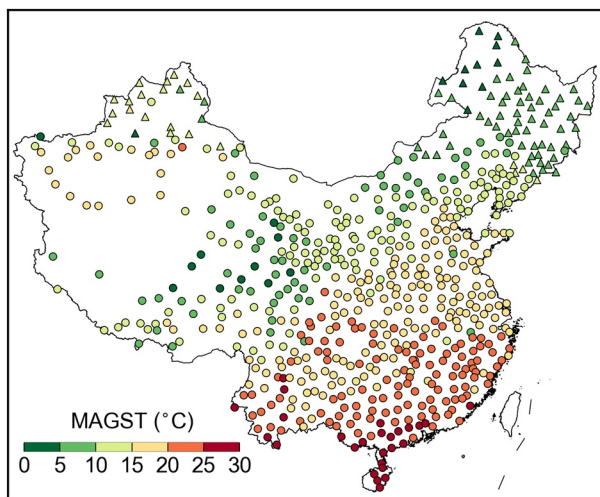
4.2. Ground Surface Temperature Over China

4.2.1. Spatial Variability of Ground Surface Temperature

The MAGST (as the mean of 1981–2010) ranges from 0.4 to 30.8°C, with a mean of 15.0 ± 6.0°C (Figure 6). The mean MAGST is about 7.8 ± 2.9°C and 16.3 ± 5.5°C for the snow-covered and snow-free sites, respectively. Given the fact that vegetation cover is absent at the CMA station, it is not surprising that the MAGST is dominated by the mean annual air temperature (MAAT) ($R^2 = 0.94$) at the snow-free sites. At the snow-covered sites, however, snow cover plays a key role in the soil thermal state, due to the snow insulation effects. The results obtained in this study indicate that an increase in HS of 10 cm corresponds to an increase of 1.7°C in MAGST (Equation 16, $P < 0.01$), which has the same effect as an increase in MAAT of 1.8°C. The model was fitted using the measurements from 91 snow-covered sites during the measurement period of 1981–2010 and has an R^2 of 0.83.

$$MAGST = 0.96 \cdot MAAT + 0.17 \cdot HS + 2.9 \tag{16}$$

The strong effect of snow insulation can also be reflected by the SO changes with a certain snow depth. The segmented linear model showed that a change in HS of 10 cm leads to a variation of 4.2°C in SO (Figure 7). SO is maintained at around 13.1 ± 0.9°C after the HS exceeds approximately 28.0 cm, indicating that snow insulation is only slightly affected by T_a variation beyond the threshold. We acknowledge that such a snow depth threshold is highly spatially variable, depending on the snow properties (e.g., snow density), climate (e.g., radiation and wind), and surface conditions (e.g., vegetation) (e.g., Domine et al., 2022; Wang et al., 2016; Zhang et al., 2021). This highlights the fact that correction of CMA T_s records is an essential step to produce consistent long-term time series and to improve understanding of soil climatology in China.


Figure 6. Simulated mean annual ground surface temperature (MAGST) across China for 1981–2010.

4.2.2. Temporal Changes of Ground Surface Temperature

Overall, the MAGST across China showed a significant warming trend with a rate of 0.20 ± 0.02°C dec^{-1} during 1956–2022, although there was strong spatial variability among the stations (std. = 0.11°C dec^{-1}, Table 2, Figures 8a and 9b). It is clear that the MAGST change was consistent with MAAT (0.23 ± 0.02°C dec^{-1}) (Figures 8a and 9a). The overall MAGST time series shows a very pronounced interdecadal variability corresponding to the MAAT cooling throughout approximately 1956–1969 (-0.50 ± 0.15°C dec^{-1}), and then continuous warming (0.30 ± 0.02°C dec^{-1}) after that. While the MAGST at the snow-free sites shows a similar interdecadal variability to the overall changes, no significant MAGST trend is apparent for the snow-covered sites before 1970, due to the stable MAAT and HS.

At the snow-covered sites, T_s always shows a more dramatic warming rate compared with the snow-free sites, and this is especially true in winter (Figures 10a and 10b, Table 2). For example, the overall mean T_s warming trend is about 0.24°C dec^{-1} (or 70.6%) higher than the T_a during 1970–2022 (Table 2). Meanwhile, the HS increases at a rate of 0.8 cm dec^{-1} (Figure 10c). The following linear model was used to predict the seasonal T_s changes (T'_s)
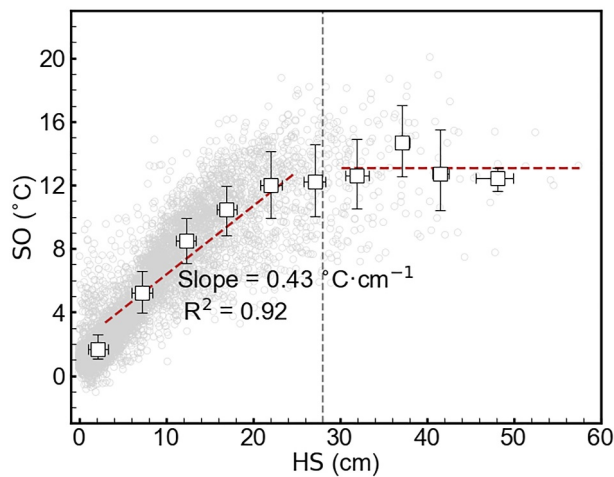
Figure 7. The influence of snow depth (HS) on the surface offset (SO) in winter (DJF) derived from the snow-covered sites during 1956–2022. The boxes represent the median SO grouped by snow depth, with an interval of 5 cm, while the short solid lines represent the 25% and 75% quartiles. A breakpoint regression (red dashed line) was applied to model the influence of HS on the SO, and delineates sites where SO is increased by HS and those where it is not, as either below or above the breakpoint (vertical dashed line).

in winter using the trends of T_a (T_a') and snow depth (HS') as predictor variables:

$$T_s' = 0.29 \cdot T_a' + 0.40 \cdot HS' + 0.13 \qquad (17)$$

The model was fitted using the measurements from 91 snow-covered sites during the measurement period of 1970–2022 and has an R^2 of 0.61. Both predictors are found to be statistically significant at $P < 0.01$. The results indicate that air temperature and snow depth both influenced the changes of T_s. An increased snow depth enhances the effect of snow insulation and amplifies the warming trend in T_s (Figures 7 and 10). In winter, an increase trend of $1.00°C \ dec^{-1}$ in mean T_a corresponds to an increase of $0.29°C \ dec^{-1}$ in mean T_s trend, and an increase trend of $1.0 \ cm \ dec^{-1}$ in HS corresponds to an increase of $0.40°C \ dec^{-1}$ in the mean T_s trend. As a reference, the T_s ($0.27 \pm 0.02°C \ dec^{-1}$) at snow-free sites shows a warming rate that is close to the T_a ($0.33 \pm 0.02°C \ dec^{-1}$) (Table 2, Figure 8b).

5. Discussion

### 5.1. Observation Uncertainties

In the early stage of establishment (1950–1960), the CMA stations were sited in suburban areas to avoid the disturbance of human activities. However, the neighboring regions of many CMA stations were changed to urban due to the rapid urban expansion since the 1970s (Wang et al., 2015). This unnatural change can amplify T_s warming (Hua et al., 2008; Ren et al., 2008; Tang et al., 2011). Previous studies found that the effect of urbanization on MAAT warming could be up to 0.07–$0.16°C \ dec^{-1}$, depending on the size of the city (Ren et al., 2008). However, quantifying such an influence at each site is challenging.

Table 2
Changes of Mean Annual and Seasonal Ground Surface Temperature (T_s, °C dec^{-1}), Air Temperature (T_a, °C dec^{-1}), and Snow Depth (HS, cm dec^{-1})

	Overall	Snow-covered			Snow-free		
	Annual	Annual	DJF	JJA	Annual	DJF	JJA
1956–2022							
T_a	0.23 ± 0.02	0.30 ± 0.03	0.35 ± 0.08	0.20 ± 0.03	0.13 ± 0.03	0.20 ± 0.05	Not significant
T_s	0.20 ± 0.02	0.35 ± 0.03	0.61 ± 0.08	0.20 ± 0.03	0.11 ± 0.03	0.14 ± 0.05	Not significant
HS	–	Not significant			–	–	–
1956–1969							
T_a	−0.64 ± 0.13	Not significant			−0.96 ± 0.12	−1.20 ± 0.39	−0.92 ± 0.14
T_s	−0.50 ± 0.15	Not significant			−0.80 ± 0.13	−1.24 ± 0.36	−0.62 ± 0.16
HS	–	Not significant			–	–	–
1970–2022							
T_a	0.34 ± 0.03	0.37 ± 0.05	0.34 ± 0.14	0.30 ± 0.05	0.33 ± 0.02	0.34 ± 0.07	0.27 ± 0.03
T_s	0.30 ± 0.02	0.40 ± 0.04	0.58 ± 0.12	0.27 ± 0.05	0.27 ± 0.02	0.26 ± 0.06	0.23 ± 0.03
HS	–	0.8 ± 0.3			–	–	–

Note. DJF means December to February, and JJA means June to August.
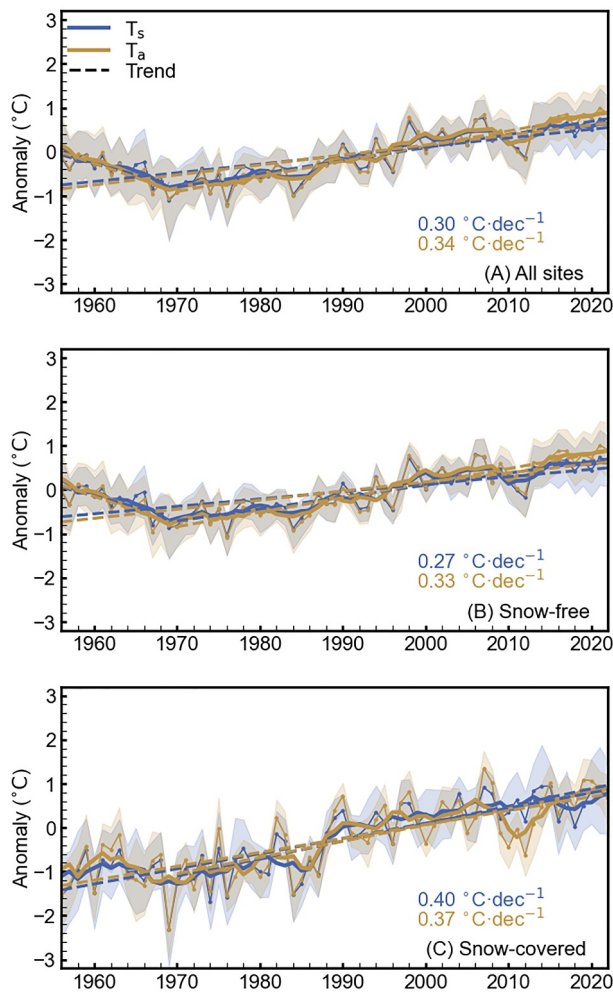
Figure 8. The overall mean annual ground surface temperature (MAGST) and mean annual air temperature (MAAT) anomaly at all sites (a), snow-free sites (b), and snow-covered sites (c). The shadow is the annual anomaly uncertainty of ±1 standard deviation, the bolded curve represents the 5-year smoothing of the original annual anomaly, and the dotted line represents the original data. Only the trends for 1970–2022 are marked in the figure, and the full trends can be found in Table 2. All the trends are found to be significant at $P < 0.01$.

According to the Surface Meteorological Observation (China) Specifications (CMA, 2013), T_s is obtained from the bare ground. The simulation conducted in this study followed this principle and used the parameterization for bare ground. In such a case, the influence of vegetation on T_s cannot be reflected by the corrected T_s present here. This also partly explains the more dramatic T_s warming in China compared to vegetation-cover areas (Qian et al., 2011).

5.2. Model Uncertainties

A consistent soil moisture was assumed over time in the process-based model. This is a significant drawback and may introduce uncertainty in the T_s simulations. Wang et al. (2011) reported a gradual drought trend over China since 1950. This means the T_s warming trend is likely underestimated due to weaker soil evaporation introduced by soil moisture decline (Long & Ren, 2023). To reduce the significant uncertainties of satellite-based soil moisture, the ensemble mean of the six widely used products was used here. However, due to the lack of in situ observations, the suitability of the soil moisture and the uncertainty introduced in T_s could not be assessed in this study. The static hydrology is considered reasonable to avoid uncertainties of soil moisture introduced by precipitation of the reanalyzes and high computational cost of water balance (Zhou et al., 2017).

Snow density is controlled by a range of complex mechanisms, which depend upon, for example, the atmospheric conditions (wind speed and radiation), topography (slope aspect), surface characteristics (vegetation and roughness), and retained liquid water (Cao et al., 2020; Lynch-Stieglitz, 1994). Snow density is hence strongly variable in both time and space (Zhong et al., 2014). Unfortunately, previous studies reported that the snow density at the CMA stations was not reliable (Kinar & Pomeroy, 2015; Zhong, Zhang, Su, et al., 2021). Therefore, we used a constant snow density of 200 kg m^{-3} throughout the snow processes based on stand-alone in situ measurements (Zhong, Zhang, Kang, & Wang, 2021). We acknowledge that the snow density used here was overestimated during the snow accumulation period and underestimated during the snow-melt period due to the snow thermal metamorphism as well as the presence of liquid water. We hence expect that the simulated T_s was too cold in autumn and too warm in late winter, although the results were found to be reasonable in representing the insulating effect of snow (Figure 4c).

5.3. Comparisons With Previous Results and Implications

The T_s has been extensively investigated based on CMA observations (Li et al., 2024; Wang et al., 2018; Zhang et al., 2016), however, many of the previous studies overestimated the warming trend without considering the change of measurement systems. For example, Wang et al. (2018) reported that the winter minimum T_s increased at a rate of 1.1°C dec^{-1} during 1965–2014 with an artificial amplified warming rate of 2.8°C dec^{-1} from 1999 to 2014, during which the measurement system was switched (Cui et al., 2020). Wang et al. (2017) showed a more pronounced MAGST warming trend (about 0.41°C dec^{-1} during 1970–2015) compared with the estimation present here. In addition, some previous studies significantly underestimated the difference between MAAT and MAGST without considering the snow insulation effects raised from inconsistency measurements (e.g., Liao et al., 2019; Wang et al., 2017). On the other hand, recent analyses based on a homogenized data set revealed that the trend of MAGST in China was approximately 0.27°C dec^{-1} from 1961 to 2016 (Long & Ren, 2023; Xu et al., 2019), which is highly aligned with
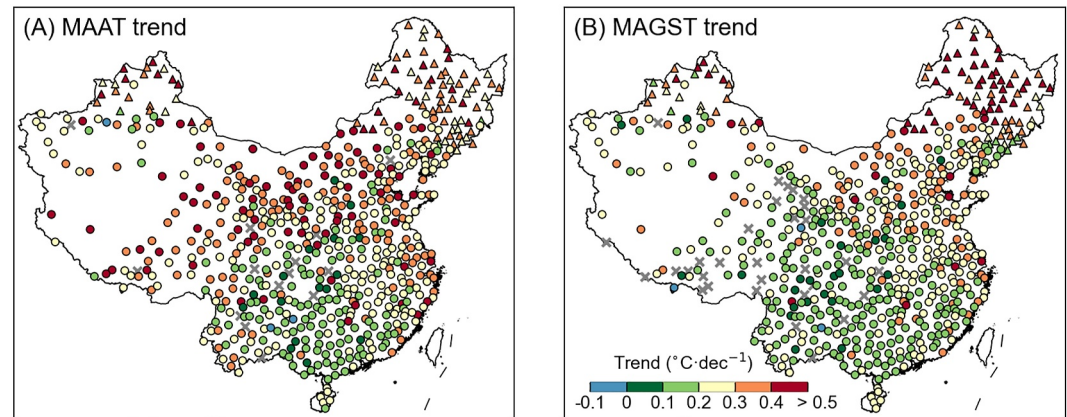
Figure 9. Estimated trends for the mean annual air temperature (MAAT) (a) and mean annual ground surface temperature (MAGST) (b) during 1956–2022. The triangle and circle symbols indicate that the trend passes the significance test ($P < 0.05$) at the snow-covered and snow-free sites, respectively, and the cross symbols indicate that the trend does not pass the significance test.

our results (i.e., 0.30°C dec^{-1} for 1970–2022). We hence strongly suggest that future studies revisit the warming T_s trend by using consistent records.

Our results indicate the MAAT dominated the MAGST at snow-free sites due to the absence of vegetation cover, which is highly consistent with previous studies (i.e., Du et al., 2017; He & Wang, 2020). On the other hand, T_s warming at the snow-covered sites was amplified by the increased snow depth (Zhou et al., 2020). While the snow depth changes are found to be a highly spatial variable (Zhong, Zhang, Kang, & Wang, 2021), understanding the soil climatology under a warming climate requires comprehensive observations and state-of-the-art models.

6. Conclusions

Ground surface temperature is widely investigated as an indicator to understand the thermal state of soil. In this study, we filled the gaps in ground surface temperature records that have arisen from the inconsistent measurements and produced long-term records for 1956–2022 for the CMA stations based on a process-based model. We then investigated the ground surface soil climatology across China based on the consistent records. The main outcomes are:

1. The simulated ground surface temperature agrees with observations well, with an RMSE of about 1.5°C for the MAGST. This indicates that the process-based model combined with downscaled reanalysis forcing is a suitable way to produce consistent ground surface temperature records.
2. The MAGST (as the mean of 1981–2010) ranged from 0.4 to 30.8°C, with a mean of 15.0 ± 6.0°C at the 632 CMA stations over China. The MAGST was mainly controlled by MAAT and additionally refined by snow depth. An increase in snow depth of 10 cm or MAAT of 1.8°C corresponds to an increase of 1.7°C in MAGST.
3. Ground surface temperature across China showed a significant overall increase of 0.20 ± 0.02°C dec^{-1} for 1956–2022. There was pronounced interdecadal variability for MAGST, cooling throughout 1956–1969 (−0.50 ± 0.15°C dec^{-1}), and then continuous warming after this date (0.30 ± 0.02°C dec^{-1}).
4. Ground surface temperature warming was amplified by the increased snow depth. At the snow-covered sites, the ground surface temperature in winter increased by about 0.24°C dec^{-1} (or 70.6%) faster than the surface air temperature, while the trend was very close in snow-free sites and during the warm seasons.
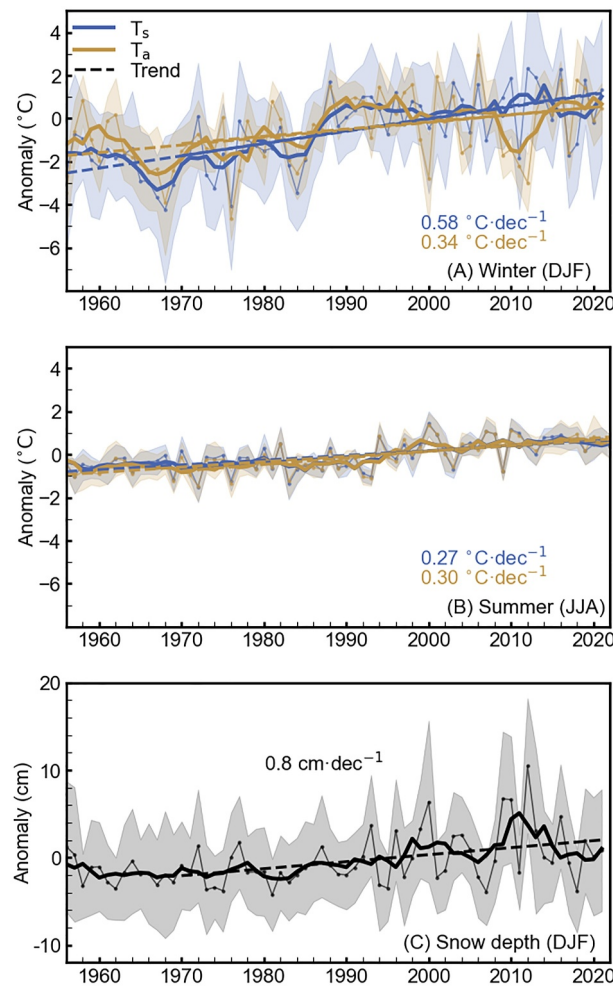
Figure 10. Anomaly of the mean ground surface temperature (T_s) and mean air temperature (T_a) at the snow-covered sites in winter (DJF) (a) and summer (JJA) (b). Anomaly of the mean snow depth at snow-covered sites in winter (DJF) (c). The shadow is the annual anomaly uncertainty of ±1 standard deviation, the bolded curve represents the 5-year smoothing of the original annual anomaly, and the dotted line represents the original data. Only the trends for 1970–2022 are marked in the figure, and the full trends can be found in Table 2. All the trends are found to be significant at $P < 0.01$.

Appendix A: Nomenclature

The following table provides the definitions of symbols used in this study (Table A1).

Table A1
Table of Symbols and Variables for This Study

Symbol	Name	Value or range	Unit
T_a	Near-surface air temperature		°C
airP	Near-surface air pressure		Pa
T_s	Ground surface temperature		°C
T_s^{mod}	Simulated ground surface temperature		°C
T_s^{obs}	Observed ground surface temperature		°C
MAAT	Mean annual air temperature		°C
MAGST	Mean annual ground surface temperature		°C
SO	Surface offset		°C

Table A1
Continued

Symbol	Name	Value or range	Unit
HS	Snow depth		cm
α	Land surface albedo		Dimensionless
α_b	Bare ground surface albedo	0.20	Dimensionless
α_{sn}	Snow surface albedo	0.50–0.85	Dimensionless
LW_d	Downwelling longwave radiation		W m^{-2}
SW_d	Downwelling shortwave radiation		W m^{-2}
LW_u	Emitted longwave radiation		W m^{-2}
Q_h	Sensible heat flux		W m^{-2}
Q_e	Latent heat flux		W m^{-2}
Q_c	Conduction heat through the snow cover of ground surface		W m^{-2}
ϵ	Ground surface emissivity		Dimensionless
σ	Stefan-Boltzmann constant	5.67×10^{-8}	W m^{-1} K^{-4}
T_{s0}	The soil temperature of the first layer of discretized soil profiles		K
ρ_a	Air density		kg m^{-3}
ρ_{sn}	Snow density	200	kg m^{-3}
ρ_i	Ice density	920	kg m^{-3}
C_p	Specific heat of air	1003.5	J K^{-1} kg^{-1}
D_h	Exchange coefficients for sensible heat		Dimensionless
α_{pt}	Priestley–Taylor coefficient for bare ground	0–1.04	Dimensionless
Δ	Slope of the saturation vapor pressure-temperature curve		Dimensionless
γ	Psychrometric constant		Dimensionless
θ_w	Soil moisture		%
θ_c	Soil critical moisture level	30	%
θ_p	Soil moisture wilting point	5	%
z_0	Depth of measured ground surface temperature		m
x	Depth from the ground surface downward		m
λ_{sn}	Snow thermal conductivity		W m^{-1} K^{-1}
λ_s	Soil thermal conductivity		W m^{-1} K^{-1}
λ_i	Ice thermal conductivity	2.2	W m^{-1} K^{-1}
λ_a	Air thermal conductivity	0.025	W m^{-1} K^{-1}
λ_w	Water thermal conductivity	0.56	W m^{-1} K^{-1}
λ_m	Soil mineral thermal conductivity	2.92	W m^{-1} K^{-1}
C	Apparent soil volumetric heat capacity		J m^{-3} K^{-1}
C_s	Soil volumetric heat capacity		J m^{-3} K^{-1}
C_i	Ice volumetric heat capacity	2.05×10^6	J m^{-3} K^{-1}
C_a	Air volumetric heat capacity	1297	J m^{-3} K^{-1}
C_w	Water volumetric heat capacity		J m^{-3} K^{-1}
C_m	Soil mineral volumetric heat capacity		J m^{-3} K^{-1}
L	Volumetric latent heat of melting for ice		J m^{-3}
θ_i	Soil ice content		%
θ_a	Soil air content	5	%
θ_{sat}	Saturated soil moisture		%
θ_m	Soil mineral content		%

Table A1
Continued

Symbol	Name	Value or range	Unit
g	Acceleration due to gravity	9.8	m s^{-2}
ψ_{sat}	Saturated soil matric potential depending on the soil texture		Dimensionless
b	The Clapp–Hornberger parameter		Dimensionless
T_{frz}	Freezing point temperature	273.15	K

Conflict of Interest

The authors declare no conflicts of interest relevant to this study.

Data Availability Statement

The reconstructed ground surface temperature records of the China Meteorological Administration (CMA) for 1956–2022 obtained by numerical simulation are publicly available via Zenodo at https://doi.org/10.5281/zenodo.10595491 [Dataset] (Wang & Cao, 2024). The long-wave and short-wave radiation observation data are available from the National Tibetan Plateau Data Center (TPDC) at https://doi.org/10.11888/Geocry.tpdc.271107 [Dataset] (Zhao, Hu, et al., 2021) and https://doi.org/10.11888/Meteoro.tpdc.270910 [Dataset] (Ma, 2020). The ERA5 is available from the European Center for Medium-Range Weather Forecast at https://doi.org/10.24381/cds.bd0915c6 [Dataset] (Hersbach et al., 2023). The soil material property information are available at http://globalchange.bnu.edu.cn/ [Dataset] (Shangguan & Dai, 2014). The process-based model codes are available via GitHub (https://github.com/BinCAO-PF/HeatTransfer1D).

References

Barton, I. J. (1979). A parameterization of the evaporation from nonsaturated surfaces. *Journal of Applied Meteorology*, *18*(1), 43–47. https://doi.org/10.1175/1520-0450(1979)018<0043:apotef>2.0.co;2

Boike, J., Wille, C., & Abnizova, A. (2008). Climatology and summer energy and water balance of polygonal tundra in the Lena River Delta, Siberia. *Journal of Geophysical Research*, *113*(G3). https://doi.org/10.1029/2007JG000540

Brunt, D. (2011). *Physical and dynamical meteorology*. Cambridge University Press.

Burke, E. J., Zhang, Y., & Krinner, G. (2020). Evaluating permafrost physics in the Coupled Model Intercomparison Project 6 (CMIP6) models and their sensitivity to climate change. *The Cryosphere*, *14*(9), 3155–3174. https://doi.org/10.5194/tc-14-3155-2020

Cao, B., Gruber, S., & Zhang, T. (2017). REDCAPP (v1.0): Parameterizing valley inversions in air temperature data downscaled from reanalyses. *Geoscientific Model Development*, *10*, 2905–2923. https://doi.org/10.5194/gmd-10-2905-2017

Cao, B., Gruber, S., Zheng, D., & Li, X. (2020). The ERA5-Land soil temperature bias in permafrost regions. *The Cryosphere*, *14*(8), 2581–2595. https://doi.org/10.5194/tc-14-2581-2020

Cao, B., Quan, X., Brown, N., Stewart-Jones, E., & Gruber, S. (2019). GlobSim (v1.0): Deriving meteorological time series for point locations from multiple global reanalyses. *Geoscientific Model Development*, *12*(11), 4661–4679. https://doi.org/10.5194/gmd-12-4661-2019

Cao, B., Wang, S., Hao, J., Sun, W., & Zhang, K. (2023). Inconsistency and correction of manually observed ground surface temperatures over snow-covered regions. *Agricultural and Forest Meteorology*, *338*, 109518. https://doi.org/10.1016/j.agrformet.2023.109518

Cao, B., Zhang, T., Peng, X., Mu, C., Wang, Q., Zheng, L., et al. (2018). Thermal characteristics and recent changes of permafrost in the upper reaches of the Heihe River Basin, Western China. *Journal of Geophysical Research: Atmospheres*, *123*(15), 7935–7949. https://doi.org/10.1029/2018JD028442

Cao, B., Zhang, T., Wu, Q., Sheng, Y., Zhao, L., & Zou, D. (2019). Permafrost zonation index map and statistics over the Qinghai-Tibet Plateau based on field evidence. *Permafrost and Periglacial Processes*, *30*(3), 178–194. https://doi.org/10.1002/ppp.2006

Cermak, V., Bodri, L., Kresl, M., Dedecek, P., & Safanda, J. (2017). Eleven years of ground-air temperature tracking over different land cover types. *International Journal of Climatology*, *37*(2), 1084–1099. https://doi.org/10.1002/joc.4764

CMA: China Meteorological Administration. (2013). *Specifications for surface meteorological observation*. China Meteorological Press.

Cosenza, P., Guérin, R., & Tabbagh, A. (2003). Relationship between thermal conductivity and water content of soils using numerical modelling. *European Journal of Soil Science*, *54*(3), 581–588. https://doi.org/10.1046/j.1365-2389.2003.00539.x

Cui, Y., Xu, W., Zhou, Z., Zhao, C., Ding, Y., Ao, X., & Zhou, X. (2020). Bias analysis and correction of ground surface temperature observations across China. *Journal of Meteorological Research*, *34*(6), 1324–1334. https://doi.org/10.1007/s13351-020-0031-9

Dee, D. P., Uppala, S. M., Simmons, a. J., Berrisford, P., Poli, P., Kobayashi, S., et al. (2011). The ERA-interim reanalysis: Configuration and performance of the data assimilation system. *Quarterly Journal of the Royal Meteorological Society*, *137*(656), 553–597. https://doi.org/10.1002/qj.828

Dingman, S. L. (2015). *Physical hydrology*. Waveland press.

Domine, F., Fourteau, K., Picard, G., Lackner, G., Sarrazin, D., & Poirier, M. (2022). Permafrost cooled in winter by thermal bridging through snow-covered shrub branches. *Nature Geoscience*, *15*(7), 554–560. https://doi.org/10.1038/s41561-022-00979-2

Douville, H., Royer, J. F., & Mahfouf, J. F. (1995). A new snow parameterization for the Météo-France climate model: Part I: Validation in stand-alone experiments. *Climate Dynamics*, *12*(1), 21–35. https://doi.org/10.1007/BF00208760

Du, J., Wang, K., Cui, B., & Jiang, S. (2020). Correction of Inhomogeneities in observed land surface temperatures over China. *Journal of Climate*, *33*(20), 8885–8902. https://doi.org/10.1175/JCLI-D-19-0521.1

Du, J., Wang, K., Wang, J., & Ma, Q. (2017). Contributions of surface solar radiation and precipitation to the spatiotemporal patterns of surface and air warming in China from 1960 to 2003. *Atmospheric Chemistry and Physics*, *17*(8), 4931–4944. https://doi.org/10.5194/acp-17-4931-2017

Fiddes, J., Endrizzi, S., & Gruber, S. (2015). Large-area land surface simulations in heterogeneous terrain driven by global data sets: Application to mountain permafrost. *The Cryosphere*, *9*(1), 411–426. https://doi.org/10.5194/tc-9-411-2015

Fiddes, J., & Gruber, S. (2014). TopoSCALE v.1.0: Downscaling gridded climate data in complex terrain. *Geoscientific Model Development*, *7*(1), 387–405. https://doi.org/10.5194/gmd-7-387-2014

Fisher, J. B., DeBiase, T. A., Qi, Y., Xu, M., & Goldstein, A. H. (2005). Evapotranspiration models compared on a Sierra Nevada forest ecosystem. *Environmental Modelling and Software*, *20*(6), 783–796. https://doi.org/10.1016/j.envsoft.2004.04.009

Gilichinsky, D., Barry, R. G., Bykhovets, S. S., Sorokovikov, V., Zhang, T., Zudin, S. L., & Fedorov-Davydov, D. G. (1998). A century of temperature observations of soil climate: Methods of analysis and long-term trends. In *Paper presented at proceedings of the 7th international conference on permafrost* (Vol. 57). Centre d'Etudes Nordiques, Université Laval Press Nordicana.

Gisnås, K., Westermann, S., Schuler, T. V., Litherland, T., Isaksen, K., Boike, J., & Etzelmüller, B. (2014). A statistical approach to represent small-scale variability of permafrost temperatures due to snow cover. *The Cryosphere*, *8*(6), 2063–2074. https://doi.org/10.5194/tc-8-2063-2014

Graham, R. M., Hudson, S. R., & Maturilli, M. (2019). Improved performance of ERA5 in Arctic Gateway relative to Four global atmospheric reanalyses. *Geophysical Research Letters*, *46*(11), 6138–6147. https://doi.org/10.1029/2019GL082781

He, Y., & Wang, K. (2020). Contrast patterns and trends of lapse rates calculated from near-surface air and land surface temperatures in China from 1961 to 2014. *Science Bulletin*, *65*(14), 1217–1224. https://doi.org/10.1016/j.scib.2020.04.001

He, Y., Wang, K., & Feng, F. (2021). Improvement of ERA5 over ERA-Interim in simulating surface Incident solar radiation throughout China. *Journal of Climate*, *34*(10), 3853–3867. https://doi.org/10.1175/JCLI-D-20-0300.1

Hersbach, H., Bell, B., Berrisford, P., Biavati, G., Horányi, A., Muñoz Sabater, J., et al. (2023). ERA5 hourly data on pressure levels from 1940 to present [Dataset]. *Copernicus Climate Change Service (C3S) Climate Data Store (CDS)*. https://doi.org/10.24381/cds.bd0915c6

Hersbach, H., Bell, B., Berrisford, P., Hirahara, S., Horányi, A., Muñoz-Sabater, J., et al. (2020). The ERA5 global reanalysis. *Quarterly Journal of the Royal Meteorological Society*, *146*(730), 1999–2049. https://doi.org/10.1002/qj.3803

Hjort, J., Karjalainen, O., Aalto, J., Westermann, S., Romanovsky, V. E., Nelson, F. E., et al. (2018). Degrading permafrost puts Arctic infrastructure at risk by mid-century. *Nature Communications*, *9*(1), 5147. https://doi.org/10.1038/s41467-018-07557-4

Hua, L. J., Ma, Z. G., & D, G. W. (2008). The impact of urbanization on air temperature across China. *Theoretical and Applied Climatology*, *93*(3–4), 179–194. https://doi.org/10.1007/s00704-007-0339-8

Jiang, H., Lu, N., Qin, J., & Yao, L. (2020). Hourly 5-km surface total and diffuse solar radiation in China, 2007–2018. *Scientific Data*, *7*(1), 311. https://doi.org/10.1038/s41597-020-00654-4

Jin, H., He, R., Cheng, G., Wu, Q., Wang, S., Lü, L., & Chang, X. (2009). Changes in frozen ground in the source area of the Yellow River on the Qinghai–Tibet Plateau, China, and their eco-environmental impacts. *Environmental Research Letters*, *4*, 045–206. https://doi.org/10.1088/1748-9326/4/4/045206

Kinar, N. J., & Pomeroy, J. W. (2015). Measurement of the physical properties of the snowpack. *Reviews of Geophysics*, *53*(2), 481–544. https://doi.org/10.1002/2015RG000481

Kumar, D., & Shekhar, S. (2015). Statistical analysis of land surface temperature–vegetation indexes relationship through thermal remote sensing. *Ecotoxicology and Environmental Safety*, *121*, 39–44. green Technologies for Environmental Pollution Control and Prevention (Part 1). https://doi.org/10.1016/j.ecoenv.2015.07.004

Li, N., Lan, C., Zhang, Y., & Ding, J. (2024). The synthesis of potential factors contributing to the asynchronous warming between air and shallow ground since the 2000s on the Tibetan Plateau. *Geoderma*, *441*, 116–753. https://doi.org/10.1016/j.geoderma.2023.116753

Liao, Y., Chen, D., & Liu, Q. (2019). The spatiotemporal characteristics and long-term trends of surface-air temperatures difference in China. *Climate Change Research (In Chinese)*, *15*, 374–384. https://doi.org/10.12006/j.issn.1673-1719.2018.199

Ling, F., & Zhang, T. (2004). A numerical model for surface energy balance and thermal regime of the active layer and permafrost containing unfrozen water. *Cold Regions Science and Technology*, *38*, 1–15. https://doi.org/10.1016/S0165-232X(03)00057-0

Long, Y., & Ren, G. (2023). Spatio-temporal patterns of warm-Season ground surface temperature-surface air temperature difference over China Mainland. *Land*, *12*(5), 1057. https://doi.org/10.3390/land12051057

Lynch-Stieglitz, M. (1994). The development and validation of a Simple snow model for the GISS GCM. *Journal of Climate*, *7*(12), 1842–1855. https://doi.org/10.1175/1520-0442(1994)007¡1842:TDAVOA¿2.0.CO;2

Ma, Y. (2020). A long-term dataset of integrated land-atmosphere interaction observations on the Tibetan Plateau (2005-2016) [Dataset]. *National Tibetan Plateau / Third Pole Environment Data Center*. https://doi.org/10.11888/Meteoro.tpdc.270910

Ma, Y., Hu, Z., Xie, Z., Ma, W., Wang, B., Chen, X., et al. (2020). A long-term (2005–2016) dataset of hourly integrated land–atmosphere interaction observations on the Tibetan Plateau. *Earth System Science Data*, *12*(4), 2937–2957. https://doi.org/10.5194/essd-12-2937-2020

Magnússon, R., Hamm, A., Karsanaev, S. V., Limpens, J., Kleijn, D., Frampton, A., et al. (2022). Extremely wet summer events enhance permafrost thaw for multiple years in Siberian tundra. *Nature Communications*, *13*(1), 1556. https://doi.org/10.1038/s41467-022-29248-x

Martens, B., Miralles, D. G., Lievens, H., van der Schalie, R., De Jeu, R. A. M., Fernández-Prieto, D., et al. (2017). GLEAM v3: Satellite-based land evaporation and root-zone soil moisture. *Geoscientific Model Development*, *10*(5), 1903–1925. https://doi.org/10.5194/gmd-10-1903-2017

Martin, L. C. P., Westermann, S., Magni, M., Brun, F., Fiddes, J., Lei, Y., et al. (2023). Recent ground thermo-hydrological changes in a southern Tibetan endorheic catchment and implications for lake level changes. *Hydrology and Earth System Sciences*, *27*(24), 4409–4436. https://doi.org/10.5194/hess-27-4409-2023

Miralles, D. G., Holmes, T. R. H., De Jeu, R. A. M., Gash, J. H., Meesters, A. G. C. A., & Dolman, A. J. (2011). Global land-surface evaporation estimated from satellite-based observations. *Hydrology and Earth System Sciences*, *15*(2), 453–469. https://doi.org/10.5194/hess-15-453-2011

Niu, G., & Yang, Z. (2006). Effects of frozen soil on snowmelt runoff and soil water storage at a continental scale. *Journal of Hydrometeorology*, *7*(5), 937–952. https://doi.org/10.1175/JHM538.1

Peng, X., Zhang, T., Frauenfeld, O. W., Wang, K., Cao, B., Zhong, X., et al. (2017). Response of seasonal soil freeze depth to climate change across China. *The Cryosphere*, *11*(3), 1059–1073. https://doi.org/10.5194/tc-11-1059-2017

Priestley, C. H. B., & Taylor, R. J. (1972). On the assessment of surface heat flux and evaporation using large-scale parameters. *Monthly Weather Review*, *100*(2), 81–92. https://doi.org/10.1175/1520-0493(1972)100¡0081:OTAOSH¿2.3.CO;2

Purdy, A. J., Fisher, J. B., Goulden, M. L., Colliander, A., Halverson, G., Tu, K., & Famiglietti, J. S. (2018). SMAP soil moisture improves global evapotranspiration. *Remote Sensing of Environment*, *219*, 1–14. https://doi.org/10.1016/j.rse.2018.09.023

Qian, B., Gregorich, E. G., Gameda, S., Hopkins, D. W., & Wang, X. L. (2011). Observed soil temperature trends associated with climate change in Canada. *Journal of Geophysical Research*, *116*(D02), 106. https://doi.org/10.1029/2010JD015012

Ren, G., Zhou, Y., Chu, Z., Zhou, J., Zhang, A., Guo, J., & Liu, X. (2008). Urbanization effects on observed surface air temperature trends in North China. *Journal of Climate*, *21*(6), 1333–1348. https://doi.org/10.1175/2007JCLI1348.1

Shangguan, W., & Dai, Y. (2014). A China dataset of soil properties for land surface modeling [Dataset]. *A Big Earth Data Platform for Three Poles*. http://globalchange.bnu.edu.cn/research/soil2/

Shangguan, W., Dai, Y., Liu, B., Zhu, A., Duan, Q., Wu, L., et al. (2013). A China data set of soil properties for land surface modeling. *Journal of Advances in Modeling Earth Systems*, *5*(2), 212–224. https://doi.org/10.1002/jame.20026

Smith, S. L., O'Neill, H. B., Isaksen, K., Noetzli, J., & Romanovsky, V. E. (2022). The changing thermal state of permafrost. *Nature Reviews Earth and Environment*, *3*(1), 10–23. https://doi.org/10.1038/s43017-021-00240-1

Streletskiy, D. A., Shiklomanov, N. I., Little, J. D., Nelson, F. E., Brown, J., Nyland, K. E., & Klene, A. E. (2017). Thaw subsidence in undisturbed tundra landscapes, barrow, Alaska, 1962-2015. *Permafrost and Periglacial Processes*, *28*(3), 566–572. https://doi.org/10.1002/ppp.1918

Sun, W., Zhang, T., Clow, G. D., Sun, Y., Zhao, W., Liang, B., et al. (2022). Observed permafrost thawing and disappearance near the altitudinal limit of permafrost in the Qilian Mountains. *Advances in Climate Change Research*, *13*(5), 642–650. https://doi.org/10.1016/j.accre.2022.08.004

Tang, C.-s., Shi, B., Gao, L., Daniels, J. L., Jiang, H., & Liu, C. (2011). Urbanization effect on soil temperature in Nanjing, China. *Energy and Buildings*, *43*(11), 3090–3098. https://doi.org/10.1016/j.enbuild.2011.08.003

Tang, W., He, J., Qi, J., & Yang, K. (2023). A dense station-based, long-term and high-accuracy dataset of daily surface solar radiation in China. *Earth System Science Data*, *15*(10), 4537–4551. https://doi.org/10.5194/essd-15-4537-2023

Tarek, M., Brissette, F. P., & Arsenault, R. (2020). Evaluation of the ERA5 reanalysis as a potential reference dataset for hydrological modelling over North America. *Hydrology and Earth System Sciences*, *24*(5), 2527–2544. https://doi.org/10.5194/hess-24-2527-2020

Walter, M. T., Brooks, E. S., McCool, D. K., King, L. G., Molnau, M., & Boll, J. (2005). Process-based snowmelt modeling: Does it require more input data than temperature-index modeling? *Journal of Hydrology*, *300*(1–4), 65–75. https://doi.org/10.1016/j.jhydrol.2004.05.002

Wang, A., Lettenmaier, D. P., & Sheffield, J. (2011). Soil moisture drought in China, 1950–2006. *Journal of Climate*, *24*(13), 3257–3271. https://doi.org/10.1175/2011JCLI3733.1

Wang, K., Zhang, T., & Zhong, X. (2015). Changes in the timing and duration of the near-surface soil freeze/thaw status from 1956 to 2006 across China. *The Cryosphere*, *9*(3), 1321–1331. https://doi.org/10.5194/tc-9-1321-2015

Wang, L., Henderson, M., Liu, B., Shen, S., Chen, X., Lian, L., & Zhou, D. (2018). Maximum and minimum soil surface TemperatureTrends over China, 1965–2014. *Journal of Geophysical Research: Atmospheres*, *123*(4), 2004–2016. https://doi.org/10.1002/2017JD027283

Wang, S., & Cao, B. (2024). Consistent ground surface temperature records for the CMA stations over China for 1956–2022 via numerical simulation [Dataset]. *Zenodo*. https://doi.org/10.5281/zenodo.10595491

Wang, W., Rinke, A., Moore, J. C., Ji, D., Cui, X., Peng, S., et al. (2016). Evaluation of air–soil temperature relationships simulated by land surface models during winter across the permafrost region. *The Cryosphere*, *10*(4), 1721–1737. https://doi.org/10.5194/tc-10-1721-2016

Wang, Y., Hu, Z.-Z., & Yan, F. (2017). Spatiotemporal variations of differences between surface air and ground temperatures in China. *Journal of Geophysical Research: Atmospheres*, *122*(15), 7990–7999. https://doi.org/10.1002/2016JD026110

Westermann, S., Langer, M., Boike, J., Heikenfeld, M., Peter, M., Etzelmüller, B., & Krinner, G. (2016). Simulating the thermal regime and thaw processes of ice-rich permafrost ground with the land-surface model CryoGrid 3. *Geoscientific Model Development*, *9*(2), 523–546. https://doi.org/10.5194/gmd-9-523-2016

Xu, W., Sun, C., Zuo, J., Ma, Z., Li, W., & Yang, S. (2019). Homogenization of monthly ground surface temperature in China during 1961–2016 and performances of GLDAS reanalysis products. *Journal of Climate*, *32*(4), 1121–1135. https://doi.org/10.1175/JCLI-D-18-0275.1

Zhang, H., Wang, E., Zhou, D., Luo, Z., & Zhang, Z. (2016). Rising soil temperature in China and its potential ecological impact. *Scientific Reports*, *6*, 1–8. https://doi.org/10.1038/srep35530

Zhang, H., Zhang, F., Zhang, G., Che, T., & Yan, W. (2018). How accurately can the air temperature lapse rate over the Tibetan plateau Be estimated from MODIS LSTs? *Journal of Geophysical Research: Atmospheres*, *123*(8), 1–18. https://doi.org/10.1002/2017JD028243

Zhang, K., Li, X., Zheng, D., Zhang, L., & Zhu, G. (2022). Estimation of global irrigation water use by the integration of multiple satellite observations. *Water Resources Research*, *58*(3), 1–23. https://doi.org/10.1029/2021WR030031

Zhang, T. (2005). Influence of the seasonal snow cover on the ground thermal regime: An overview. *Reviews of Geophysics*, *43*(4). https://doi.org/10.1029/2004RG000157

Zhang, T., & Zhong, X. (2014). Classification and regionalization of the seasonal snow cover across the Eurasian Continent. *Journal of Glaciology and Geocryology*, *36*, 933.

Zhang, W., Shen, Y., Wang, X., Kang, S., Chen, A., Mao, W., & Zhong, X. (2021). Snow cover controls seasonally frozen ground regime on the southern edge of Altai Mountains. *Agricultural and Forest Meteorology*, *297*, 108–271. https://doi.org/10.1016/j.agrformet.2020.108271

Zhao, L., Hu, G., Zou, D., Wu, T., Du, E., Liu, G., et al. (2021). A synthesis dataset of permafrost for the Qinghai-Xizang (Tibet) Plateau, China (2002-2018) [Dataset]. *National Tibetan Plateau/Third Pole Environment Data Center*. https://doi.org/10.11888/Geocry.tpdc.271107

Zhao, L., Zou, D., Hu, G., Wu, T., Du, E., Liu, G., et al. (2021b). A synthesis dataset of permafrost thermal state for the Qinghai–Tibet (Xizang) Plateau, China. *Earth System Science Data*, *13*(8), 4207–4218. https://doi.org/10.5194/essd-13-4207-2021

Zhong, X., Zhang, T., Kang, S., & Wang, J. (2021). Snow depth trends from CMIP6 models conflict with observational evidence. *Journal of Climate*, *35*(4), 1293–1307. https://doi.org/10.1175/jcli-d-21-0177.1

Zhong, X., Zhang, T., & Wang, K. (2014). Snow density climatology across the former USSR. *The Cryosphere*, *8*(2), 785–799. https://doi.org/10.5194/tc-8-785-2014

Zhong, X. Y., Zhang, T., Su, H., Xiao, X. X., Wang, S. F., Hu, Y. T., et al. (2021). Impacts of landscape and climatic factors on snow cover in the Altai Mountains, China. *Advances in Climate Change Research*, *12*(1), 95–107. https://doi.org/10.1016/j.accre.2021.01.005

Zhou, C., Wang, K., & Ma, Q. (2017). Evaluation of eight current reanalyses in simulating land surface temperature from 1979 to 2003 in China. *Journal of Climate*, *30*(18), 7379–7398. https://doi.org/10.1175/JCLI-D-16-0903.1

Zhou, Y., Gao, X., Zhang, K., Li, Y., & Yang, L. (2020). Spatiotemporal variations in 3.2 m soil temperature in China during 1980–2017. *Climate Dynamics*, *54*(1–2), 1233–1244. https://doi.org/10.1007/s00382-019-05055-x

Zhu, F., Li, X., Qin, J., Yang, K., Lan, C., Tang, W., & Shen, C. (2021). Integration of multisource data to estimate downward longwave radiation based on deep neural networks. *IEEE Transactions on Geoscience and Remote Sensing*, *60*, 1–15. https://doi.org/10.1109/TGRS.2021.3094321

Zwieback, S., Westermann, S., Langer, M., Boike, J., Marsh, P., & Berg, A. (2019). Improving permafrost modeling by assimilating remotely sensed soil moisture. *Water Resources Research*, *55*(3), 1814–1832. https://doi.org/10.1029/2018WR02324